

Fourier-Domain Multichannel Autofocus for Synthetic Aperture Radar

Kuang-Hung Liu, *Student Member, IEEE*, and David C. Munson, Jr., *Fellow, IEEE*

Abstract—Synthetic aperture radar (SAR) imaging suffers from image focus degradation in the presence of phase errors in the received signal due to unknown platform motion or signal propagation delays. We present a new autofocus algorithm, termed Fourier-domain multichannel autofocus (FMCA), that is derived under a linear algebraic framework, allowing the SAR image to be focused in a noniterative fashion. Motivated by the multichannel autofocus (MCA) approach, the proposed autofocus algorithm invokes the assumption of a low-return region, which generally is provided within the antenna sidelobes. Unlike MCA, FMCA works with the collected polar Fourier data directly and is capable of accommodating wide-angle monostatic SAR and bistatic SAR scenarios. Most previous SAR autofocus algorithms rely on the prior assumption that radar's range of look angles is small so that the phase errors can be modeled as varying along only one dimension in the collected Fourier data. And, in some cases, implicit assumptions are made regarding the SAR scene. Performance of such autofocus algorithms degrades if the assumptions are not satisfied. The proposed algorithm has the advantage that it does not require prior assumptions about the range of look angles, nor characteristics of the scene.

Index Terms—Autofocus, bistatic SAR, multichannel autofocus, synthetic aperture radar, wide-angle SAR.

I. INTRODUCTION

SYNTHETIC aperture radar (SAR) produces high-resolution microwave images using a small antenna. High resolution in the range direction is achieved through traditional pulse compression, while high resolution in the cross-range direction is obtained by illuminating the target from many viewing angles. In one form of SAR, termed *spotlight mode*, the radar antenna is continuously steered to illuminate the target with each transmitted microwave pulse. When the same antenna is used for both transmitting and receiving, it is referred to as *monostatic* SAR, while *bistatic* SAR uses separate antennas for transmitting and receiving. We will focus on spotlight-mode SAR and consider both the monostatic and bistatic scenarios. The data collection in spotlight-mode SAR can be conveniently modeled using a tomographic formulation, which allows us to view returned signals as data lying in the *Fourier domain* of the target reflection,

after demodulating with a copy of the transmitted signal [1]. The locus of the data in the Fourier domain is a polar annulus and is defined by the radar waveform parameters and the radar's range of viewing angles. In principle, we can construct the SAR image using polar-to-Cartesian interpolation followed by 2-D Fourier inversion. However, due to the signal delays resulting from inaccurate range measurements or signal propagation effects, there will be a demodulation timing error at the radar receiver [2]. This will produce unknown phase errors in the collected Fourier data and cause the reconstructed image to suffer distortion. Algorithms that apply signal processing techniques to remove such undesired phase errors are called *autofocus*.

Most work on SAR autofocus algorithms has relied on the key assumption that the radar's range of viewing angles is small enough so that the phase errors can be well modeled as varying only along one Cartesian dimension in the collected Fourier data domain [2]. (This is called the small-angle assumption.) These approaches include phase-gradient autofocus (PGA) [3], [4], a standard autofocus algorithm used in practice, and multichannel autofocus (MCA) [5]. The small-angle assumption simplifies the general autofocus problem, because the unknown phase errors have only a 1-D blurring effect on the spatial-domain image. In addition, each range coordinate of the reconstructed image is defocused by the same blurring kernel. It has been found that the small-angle assumption is especially important to the MCA approach. In fact, MCA breaks down quickly when the small-angle assumption is violated [6]. Some other autofocus algorithms compensate the phase errors by maximizing the sharpness of the reconstructed image [7]–[9]. Popular metrics that measure image sharpness include entropy and various powers of the image intensity [10]. These sharpness-maximizing autofocus algorithms tend to favor sparse images such as collections of point scatterers. While the restoration results obtained using these approaches often are outstanding, the techniques sometimes fail to produce correct restorations when the underlying scene is poorly described by the implicitly assumed image model.

As explained in [5], [11] there is a multichannel nature to the autofocus problem where MCA treats the rows of the perfectly focused image as outputs of a bank of parallel filters excited by a common blurring kernel [12]. PGA takes advantage of the redundancy of the phase-error function by averaging across many rows of the image. In this paper, we exploit the multichannel nature by recognizing that the Fourier data collected for each viewing angle (data that belongs to the same cross-range coordinate) are corrupted by the same phase error, and we view the Fourier data that belong to the same range coordinate as a single channel. Although in our approach it is more complicated to express the relationship between the channels and the phase errors,

Manuscript received November 05, 2010; accepted April 08, 2011. Date of publication May 19, 2011; date of current version November 18, 2011. This work was supported in part by the National Science Foundation under Grant CCF 0430780. The associate editor coordinating the review of this manuscript and approving it for publication was Prof. Margaret Cheney.

The authors are with the Department of Electrical Engineering and Computer Science, University of Michigan, Ann Arbor, MI 48109-2122 USA (E-mail: khlui@umich.edu, munson@umich.edu).

Color versions of one or more of the figures in this paper are available online at <http://ieeexplore.ieee.org>.

Digital Object Identifier 10.1109/TIP.2011.2156421

compared to MCA and PGA, it is this Fourier-domain observation that allows our algorithm to accommodate wide-angle monostatic SAR and bistatic SAR.

We apply a subspace-based technique to the autofocus problem, where we construct a subspace where the focused image resides. The basis of this subspace is found from the corrupted Fourier data. By requiring that the underlying SAR image have a region with zero or nearly-zero pixel values, and establishing the relationship between the SAR image and the collected Fourier data, we can write a set of linear equations that allow us to determine the phase errors directly [13], [14]. The requirement for this known region with zero (or nearly zero) pixel values generally is satisfied by the low-return region within the sidelobes of the antenna pattern. In practice, this region is created by acquiring the collected returned signals with sufficiently small sample spacings in both the range and cross range directions, so that the reconstructed image has coverage extending beyond the heavily illuminated portion of the target scene determined by the antenna pattern. This linear framework allows us to determine the phase errors in a noniterative fashion, and the quality of the reconstruction does not depend on the characteristics of the underlying scene. We refer to this linear algebraic approach as *Fourier-domain multichannel autofocus* (FMCA). This paper expands upon a preliminary version of our work reported in [15].

The organization of the paper is as follows. Section II presents the autofocus problem statement. In Section III, we derive the FMCA framework and propose the procedure for image restoration. Section IV compares FMCA with MCA. Simulation results are presented in Section V. Finally, a conclusion is given in Section VI.

Throughout this paper, a capital boldface letter **A** denotes a matrix and lower-case boldface letter **a** denotes a column vector. A superscript $(\cdot)^H$ denotes the hermitian transpose. For a complex-valued vector **a**, the function $\angle(\mathbf{a})$ retains the phase part of **a**. The function $\text{Diag}(\mathbf{a})$ maps vector **a** to a diagonal matrix with the elements of **a** on the main diagonal.

II. PROBLEM FORMULATION

In this section we first briefly review the tomographic formulation of spotlight-mode SAR [2]. We then state the autofocus problem.

A. SAR Tomographic Formulation

When imaging terrain using spotlight-mode SAR, a small antenna is mounted on an aircraft or a spacecraft and is continuously steered to illuminate the scene of interest with each transmitted microwave pulse. A target scene, represented by a complex-valued reflectivity function $g(x, y)$, is illuminated by the radar over a range of viewing angles, $\theta_m : \theta_{\min} \leq \theta_m \leq \theta_{\max}$, $m = 0, 1, \dots, M-1$. The goal is to reconstruct $g(x, y)$ and display its magnitude $|g(x, y)|$. The following assumptions made throughout the paper are crucial to the problem formulation.

- *Far field assumption:* Unless otherwise specified, we assume that the radar platform operates at a standoff distance that is large compared to the target scene diameter. Under this assumption, when the transmitted radar pulse reaches

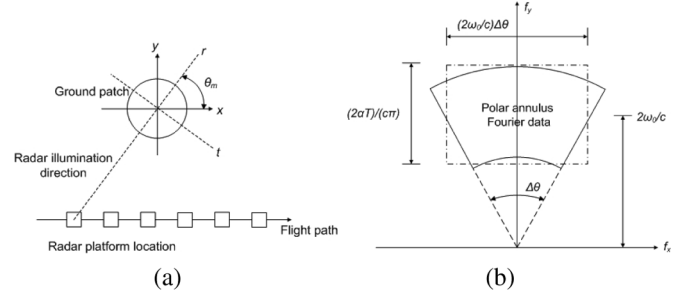


Fig. 1. (a) Monostatic SAR. (b) Collected Fourier data.

the target, it can be well approximated as having a planar wavefront.

- *Reflectivity invariance:* The target reflectivity function $g(x, y)$ is assumed to be independent of both the viewing angle and the frequency of incident radiation. These assumptions hold for moderately narrow ranges of viewing angles and for narrowband waveforms.

Using a tomographic formulation, the signal collected from viewing angle θ_m is a “slice” of the 2-D Fourier transform of $g(x, y)$, taken at angle θ_m . These signals are then assembled into a matrix $\mathbf{G}_p[m, n]$, which is the polar-format Fourier transform of $g(x, y)$. An example of a monostatic SAR system and the collected Fourier data is shown in Fig. 1, where ω_0 , α and T correspond to the center frequency, chirp rate and signal duration of the transmitted linear FM signal, respectively [1].

To reconstruct the image, it is standard to first interpolate $\mathbf{G}_p[m, n]$ to a Cartesian grid and then apply an inverse Fourier transform. We require a linear polar-to-Cartesian interpolation to preserve the linear structure for our problem. In practice, linear interpolation is almost always used; for example see [2].

The section of terrain that is imaged by a SAR depends on the antenna footprint, which is the region illuminated by the antenna beam with significant energy. Energy collected from outside the antenna footprint is small.

In the bistatic SAR scenario, separate antennas are used for transmitting microwave pulses and collecting returned signals. As an example, this scenario arises when a high-powered transmitter stands off in a safe location and the receiver covertly collects data to form the SAR image. Similar to the monostatic case, it can be shown that the demodulated collected return signal corresponds to a slice of the 2-D Fourier transform of the target terrain’s reflectivity function [16]. For the bistatic case, the angular location of the Fourier data is along the bisection angle between the transmitting antenna to the center of the scene to the receiving antenna. The collected Fourier data from all viewing angles lies on a skewed polar annulus. An example of a bistatic SAR geometry and the collected Fourier data grid is shown in Fig. 2. The image formation process is similar to the monostatic case where linear interpolation is followed by Fourier inversion.

B. Autofocus Problem

A challenge in SAR imaging is that in order to correctly demodulate the return signal, the two-way travel time of each radar pulse must be known accurately. Inaccurate time measurements due to signal propagation through media having a

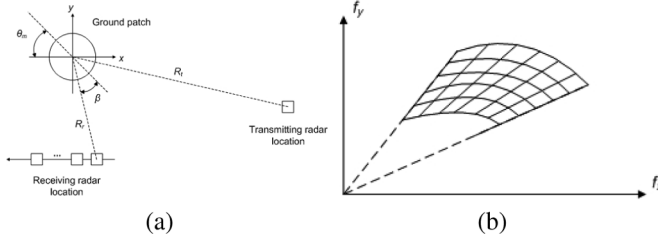


Fig. 2. (a) Bistatic SAR. (b) Collected Fourier data.

spatially-varying propagation velocity, or imprecise knowledge of the motion of the radar, will result in an undesired phase shift to each demodulated radar return. The phase corrupted data $\tilde{\mathbf{G}}_p[m, n]$ is expressed as

$$\tilde{\mathbf{G}}_p[m, n] = \mathbf{G}_p[m, n] e^{j\phi(m)} \quad (1)$$

where $\phi(m) \in \mathbb{R}$, $m = 0, 1, \dots, M-1$ are unknown. The presence of the phase errors will have the effect of convolving the spatial image with an unknown 2-D blurring kernel function and cause the reconstructed image to suffer distortion. To simplify the problem, most existing autofocus algorithms assume that the radar's range of viewing angles is small enough so that $\mathbf{G}_p[m, n]$ can be well approximated as lying on a Cartesian grid [5]. In this case, the polar-to-Cartesian interpolation process can be ignored in the image formation process and this leads to a simplified 1-D phase error model in the spatial domain,

$$\tilde{g}(x, y) = g(x, y) \otimes b(x) \quad (2)$$

where $b(x)$ represents the 1-D inverse Fourier transform of $e^{j\phi(m)}$, $\tilde{g}(x, y)$ is the defocused image and \otimes denotes M -point circular convolution. Note that each row of $\tilde{g}(x, y)$ is corrupted by the same phase error function $b(x)$. State-of-the-art techniques including PGA and MCA are developed based on this 1-D phase corruption model. Both PGA and MCA can fail to produce a focused image when the range of viewing angles is moderately wide, with MCA especially sensitive to the small angle assumption. A study of the sensitivity of MCA to the small angle assumption is provided in [6].

The autofocus problem is to estimate $\phi(m)$, given the data $\tilde{\mathbf{G}}_p[m, n]$ and assumptions about the imaging scenario. With an accurate phase estimate, we can restore the perfectly-focused image by compensating the corrupted Fourier data using the phase estimate.

III. FMCA RESTORATION FRAMEWORK

The FMCA reconstruction method assumes there exists a known region in $g(x, y)$ with pixels having nearly zero value and relates the collected Fourier data to this constraint. As shown later, FMCA expresses this relationship as a set of linear equations and solves for the unknown phase errors directly.

Let $\mathbf{G}_c[k, l]$ be Cartesian-grid Fourier data linearly interpolated from $\mathbf{G}_p[m, n]$ (assuming $\mathbf{G}_p[m, n]$ is shifted downward to baseband), where $0 \leq k \leq K-1$, $0 \leq l \leq L-1$ and K, L denotes the extent of coverage of the rectangular Fourier space

region to which we wish to interpolate. Using linear interpolation, the Cartesian grid data $\mathbf{G}_c[k, l]$ can be expressed as

$$\mathbf{G}_c[k, l] = \sum_{m, n} \alpha(k, l, m, n) \mathbf{G}_p[m, n] \quad (3)$$

where $\alpha(k, l, m, n)$ are the interpolation coefficients. In this paper, for simplicity, we use nearest-neighbor interpolation, which means that $\alpha(k, l, m, n) = 1$ when $\mathbf{G}_p[m, n]$ is closest to $\mathbf{G}_c[k, l]$ and 0 otherwise. However, in principle, any linear interpolation can be used. The image $g(x, y)$ is reconstructed by using an inverse discrete Fourier transform,

$$g(x, y) = \frac{1}{KL} \sum_{k, l} \mathbf{G}_c[k, l] e^{j2\pi(xk/K + yl/L)}. \quad (4)$$

The region of terrain that is imaged in SAR depends on the antenna pattern. Little energy is collected from outside the antenna main beam. By oversampling in both the range and cross-range directions, in principle we can produce a SAR image that has low-value pixels at the border of the image. However, the unknown phase errors introduced to the collected Fourier data will have the effect of convolving the focused image $g(x, y)$ with an unknown 2-D blurring kernel, so that the energy of $g(x, y)$ may be spread across the whole image plane. Therefore, the image constructed from the phase corrupted data $\tilde{\mathbf{G}}_c[k, l]$ may not contain a low-return region. FMCA compensates the phase errors by forcing the low-return region in the border of the reconstructed image to have nearly zero value. More generally, FMCA applies even if the region known to have low-return is not in the border of the image.

Let $g(x_r, y_r)$, $r = 0, 1, \dots, R-1$ be the set of pixels that are nearly zero. From (1), (3) and (4) we have

$$\begin{aligned} g(x_r, y_r) &= \frac{1}{KL} \sum_{k, l} \sum_{m, n} \alpha(k, l, m, n) \\ &\quad \times \tilde{\mathbf{G}}_p[m, n] e^{-j\phi(m)} e^{j2\pi(x_r k/K + y_r l/L)} \\ &\approx 0. \end{aligned} \quad (5)$$

In matrix notation, (5) can be written as

$$\mathbf{A} e^{-j\phi} \approx 0 \quad (6)$$

where $\phi = [\phi(0) \phi(1) \dots \phi(M-1)]^T$ and \mathbf{A} is an R by M matrix with elements

$$\begin{aligned} \mathbf{A}_{mr} &= \frac{1}{KL} \sum_{k, l} \left(\sum_n \alpha(k, l, m, n) \tilde{\mathbf{G}}_p[m, n] \right) e^{j2\pi(x_r k/K + y_r l/L)} \end{aligned} \quad (7)$$

where $0 \leq r \leq R-1$, $0 \leq m \leq M-1$.

Assuming that the values of $g(x_r, y_r)$'s are zero, $e^{-j\phi}$ must be in the null space of \mathbf{A} . By carefully selecting the sampling rate and the low-return region, we can ensure that \mathbf{A} has rank $M-1$ and the autofocus phase correction vector $e^{-j\phi}$ can be

obtained by determining the vector \mathbf{f} spanning the null space of \mathbf{A}

$$\mathbf{f} = \beta e^{-j\hat{\phi}} \in \text{Null}(\mathbf{A})$$

where β is an arbitrary complex constant. We retain only the phase part of \mathbf{f} as our autofocus phase estimate

$$e^{-j\hat{\phi}} = e^{j\angle \mathbf{f}}.$$

However, when $|g(x_r, y_r)| \neq 0$, due to additive noise or bright reflectors in the antenna sidelobes, we observe that \mathbf{A} has full column rank and we cannot determine $e^{-j\hat{\phi}}$ using the null space of \mathbf{A} . Although $g(x_r, y_r)$ may not have a region that is truly zero, we would like the phase estimate to produce a restored image with minimum energy in the low-return region. In other words, we wish to have a phase estimate $e^{-j\hat{\phi}_{\min}}$ such that $\hat{\phi}_{\min}$ satisfies

$$\hat{\phi}_{\min} = \arg \min_{\mathbf{a} \in \mathbb{R}^M} \|\mathbf{A} e^{-j\mathbf{a}}\|_2. \quad (8)$$

Equation (8) is very challenging to solve, and therefore we adopt the following approximation

$$e^{-j\hat{\phi}_{\min}} \approx \mathbf{v} = \arg \min_{\mathbf{a} \in \mathbb{C}^M, \|\mathbf{a}\|_2=1} \|\mathbf{A} \mathbf{a}\|_2. \quad (9)$$

The solution to (9) is given by the right singular vector that corresponds to the smallest singular value of \mathbf{A} . To ensure that \mathbf{v} has the form of $e^{-j\hat{\phi}}$ in (6), the FMCA autofocus phase estimator $\hat{\phi}_{FMCA}$ keeps only the phase part of \mathbf{v} , resulting in

$$\hat{\phi}_{FMCA} = -\angle(\mathbf{v}). \quad (10)$$

IV. COMPARISON WITH PREVIOUS METHOD

Since FMCA and MCA are designed for the same imaging scenario, it is interesting to compare these autofocus approaches. We have the following result.

Theorem 1: As the range of viewing angles approaches zero, MCA is equivalent to FMCA.

Proof: When the SAR operates over exceedingly small viewing angles, the collected polar formatted Fourier data $\tilde{\mathbf{G}}_p[m, n]$ correspond approximately to a Cartesian format $\tilde{\mathbf{G}}_c[k, l]$, and $\tilde{\mathbf{G}}_c[k, l] = \tilde{\mathbf{G}}_p[m, n]$ for $k = n, l = m$. The polar-to-Cartesian interpolation can be ignored and the elements of FMCA matrix \mathbf{A} degenerate to

$$\mathbf{A}_{rm} = \frac{1}{MN} \sum_n \tilde{\mathbf{G}}_p[m, n] e^{j2\pi(x_r m/M + y_r n/N)}. \quad (11)$$

Let \mathbf{W}_M be the M point DFT matrix ($\mathbf{W}_M[i, j] \triangleq (1/\sqrt{M})e^{-j2\pi(i-1)(j-1)/M}$, $1 \leq i, j \leq M$), \mathbf{W}_M is unitary (i.e., $\mathbf{W}_M \mathbf{W}_M^H = \mathbf{I}$). We can make the following observation for the FMCA problem (6):

$$0 \approx \mathbf{A} e^{-j\hat{\phi}} = \mathbf{A} \mathbf{W}_M \mathbf{W}_M^H e^{-j\hat{\phi}} = \mathbf{B} \mathbf{e} \quad (12)$$

where $\mathbf{e} = \mathbf{W}_M e^{-j\hat{\phi}} = \text{DFT}^{-1}(e^{-j\hat{\phi}})$ and $\mathbf{B} = \mathbf{A} \mathbf{W}_M$ is an R by M matrix with elements

$$\mathbf{B}_{mr} = \tilde{g}(\text{mod}(x_r - m, M), y_r). \quad (13)$$

Here $\text{mod}(x_r - m, M)$ denotes $(x_r - m)$ modulo M . Note that the elements of \mathbf{B} are constructed from the rows of \tilde{g} that correspond to the low-return constraint. Since the MCA framework can be stated as solving $0 \approx \mathbf{B} \mathbf{e}$ with constraints on the structure of \mathbf{e} (MCA finds the phase error function in the spatial domain) [5], we have the desired result. ■

Note that MCA also solves $0 \approx \mathbf{B} \mathbf{e}$ by using the following approximation

$$\hat{\mathbf{e}} = \arg \min_{\mathbf{a} \in \mathbb{C}^M, \|\mathbf{a}\|_2=1} \|\mathbf{B} \mathbf{a}\|_2 \quad (14)$$

and produces the phase estimates $\hat{\phi}_{MCA}$ by

$$\hat{\phi}_{MCA} = -\angle(\text{DFT}(\hat{\mathbf{e}})). \quad (15)$$

Next, we study the restoration capability of FMCA. FMCA inherits multiple properties from MCA, which we will briefly list here. The derivations are similar to those for MCA [5].

1) *Property 1 (Equivalence of Singular Values):* Let \mathbf{A} be the FMCA data matrix formed from uncorrupted data and $\tilde{\mathbf{A}}$ be the FMCA data matrix formed from corrupted data. Then the magnitudes of the singular values of \mathbf{A} and $\tilde{\mathbf{A}}$ are identical.

Property 1 is easy to see, since from (7) we have $\tilde{\mathbf{A}} = \mathbf{A} \text{Diag}(e^{j\hat{\phi}})$. Observe that

$$\tilde{\mathbf{A}}^H \tilde{\mathbf{A}} = \mathbf{A}^H \text{Diag}(e^{j\hat{\phi}})^H \text{Diag}(e^{j\hat{\phi}}) \mathbf{A} = \mathbf{A}^H \mathbf{A} \quad (16)$$

and thus \mathbf{A} and $\tilde{\mathbf{A}}$ have singular values with the same magnitudes.

2) *Property 2 (Equivalence of Restoration):* Suppose that \mathbf{A} (or equivalently $\tilde{\mathbf{A}}$) has a distinct smallest absolute singular value. Then applying the FMCA correction filter \mathbf{v} and $\tilde{\mathbf{v}}$ to \mathbf{A} and $\tilde{\mathbf{A}}$, respectively, produces the same magnitude restoration where \mathbf{v} and $\tilde{\mathbf{v}}$ are the minimum right singular vector of \mathbf{A} and $\tilde{\mathbf{A}}$ respectively, i.e.,

$$|\mathbf{A} \mathbf{v}| = |\tilde{\mathbf{A}} \tilde{\mathbf{v}}|. \quad (17)$$

To show Property 2, first use Property 1 and the assumption that the smallest absolute singular value of \mathbf{A} and $\tilde{\mathbf{A}}$ is distinct. We have

$$|\tilde{\mathbf{A}} \tilde{\mathbf{v}}| = |\mathbf{A} \text{Diag}(e^{j\hat{\phi}}) \tilde{\mathbf{v}}|. \quad (18)$$

Thus, $\mathbf{v} = \beta \text{Diag}(e^{j\hat{\phi}}) \tilde{\mathbf{v}}$, where β is a complex scalar with $|\beta| = 1$. Then we observe that

$$|\tilde{\mathbf{A}} \tilde{\mathbf{v}}| = |\beta^{-1} \mathbf{A} \text{Diag}(e^{j\hat{\phi}}) \text{Diag}(e^{j\hat{\phi}})^H \mathbf{v}| = |\mathbf{A} \mathbf{v}| \quad (19)$$

producing the desired result.

Property 2 shows that applying FMCA to the perfectly-focused image or any defocused image produces the same restored image (we are only interested in displaying the image magnitude). In other words, the restoration capability of FMCA does

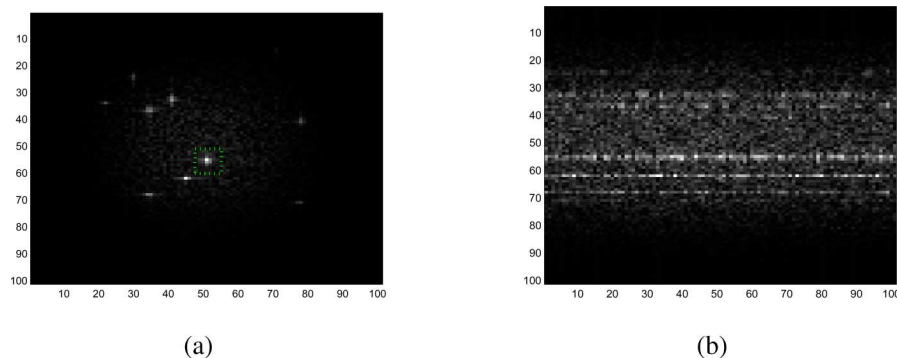


Fig. 3. Simple point target image for 0.01 degree look angle: (a) perfectly-focused image with 2-D sinc-squared antenna pattern applied, the border of the image is assumed to have low return (the cross section of the point target inside the dotted box is plotted in Fig. 7), (b) defocused image produced after applying a white phase error function.

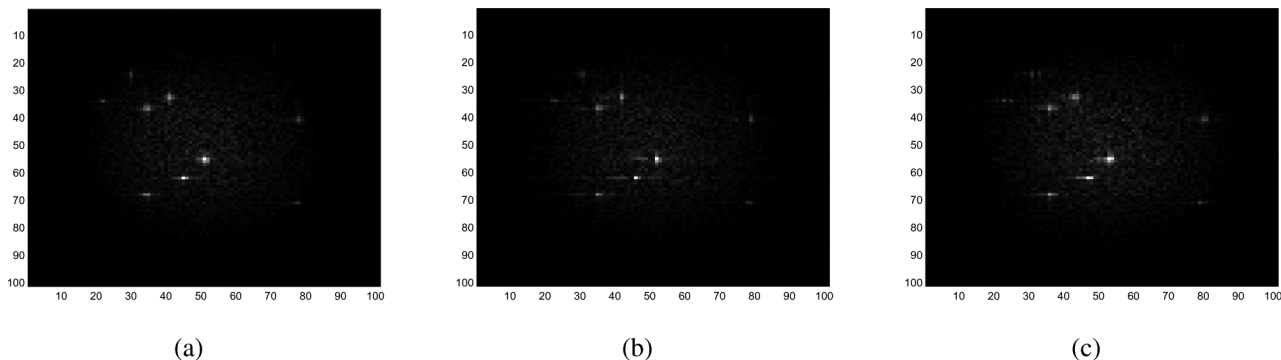


Fig. 4. Autofocus for the point target image with a 0.01 degree viewing angle: (a) image restored by FMCA, (b) image restored by MCA, (c) image restored by PGA.

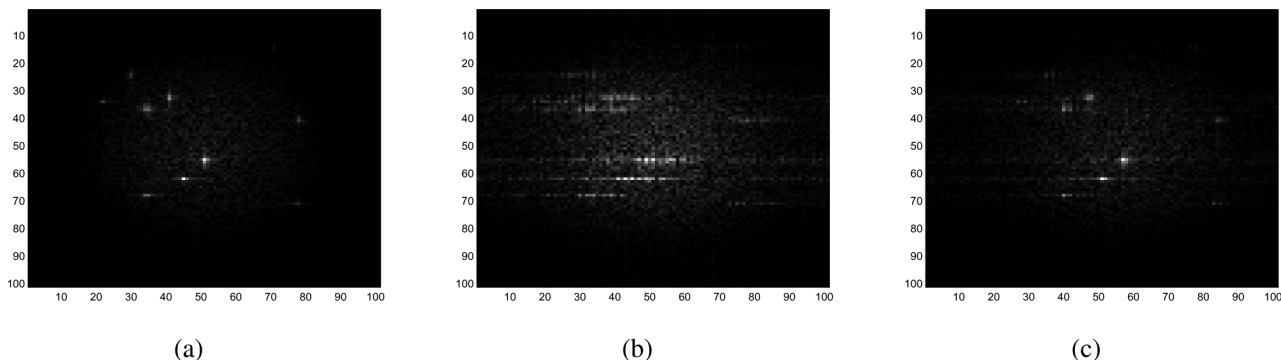


Fig. 5. Autofocus for the point target image with a 0.1 degree viewing angle: (a) image restored by FMCA, (b) image restored by MCA, (c) image restored by PGA.

not depend on the phase error function, unlike existing autofocus algorithms where the performance tends to degrade when the phase errors are large and rapidly-varying. However, this result does not imply anything about the quality of the restoration.

V. SIMULATION RESULTS

In this section, we present simulation results for FMCA image restoration for both monostatic and bistatic SAR scenarios. We compare the performance of FMCA with both MCA and PGA. An antenna pattern simulated by the main lobe of a 2-D sinc squared function was applied to the SAR images so that the border of the image had nearly zero, but non-negligible pixel magnitudes. The phase errors were *i.i.d* across the cross-range coordinate and uniformly distributed between $-\pi$ and π . This phase error model is the worst case scenario and produces the most severe defocusing effects.

A. Monostatic SAR Scenario

In the monostatic SAR scenario, we studied how the range of viewing angles affects the performance of various autofocus algorithms. To evaluate the performance of reconstruction, we first tested the three autofocus algorithms with images of randomly scattered point targets. The perfectly focused image and the phase corrupted image for a 0.01 degree range of viewing angles are shown in Fig. 3(a) and (b), respectively. The images restored by FMCA, MCA and PGA are shown in Fig. 4. In this case, the locations of the collected Fourier data closely resemble a Cartesian grid and all of the algorithms could successfully reconstruct the image. The cross section of the point target inside the dotted box in Fig. 3(a) is plotted in Fig. 7(a). We can see that all three algorithms successfully reconstructed the point target. Fig. 5 shows the image restoration results for the same point target image but with a 0.1 degree range of viewing angles. We

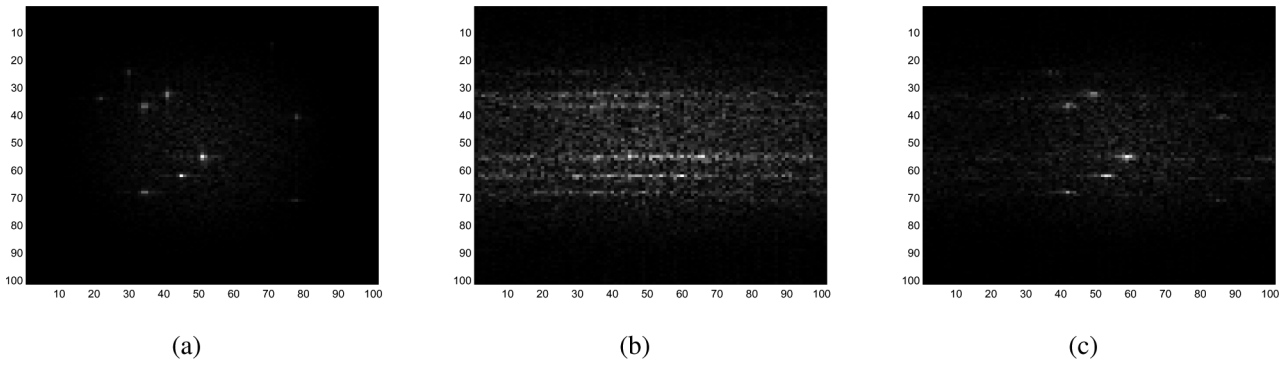


Fig. 6. Autofocus for the point target image with a 1 degree viewing angle: (a) image restored by FMCA, (b) image restored by MCA, (c) image restored by PGA.

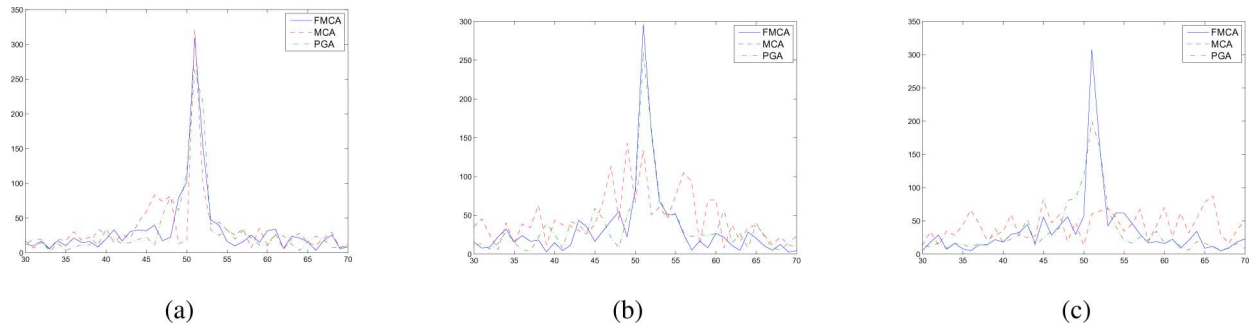


Fig. 7. Comparison of the point-target cross-sections: (a) for 0.01 degree viewing angle, (b) for 0.1 degree viewing angle, (c) for 1 degree viewing angle.

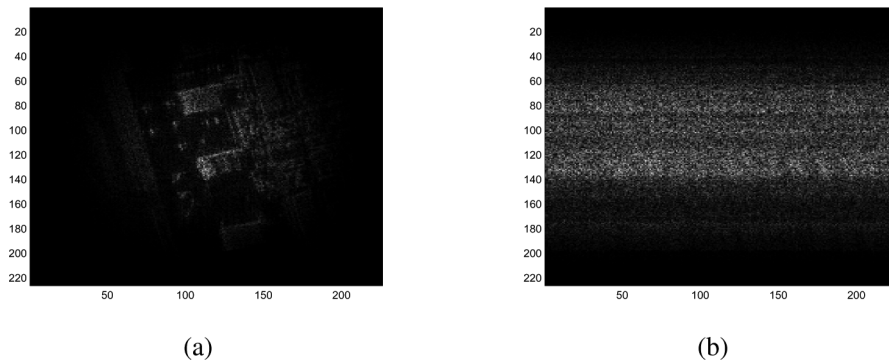


Fig. 8. A SAR image produced from experimental data with 0.005 degree viewing angle: (a) perfectly focused image with 2-D sinc-squared antenna pattern applied, the border of the image is assumed to have low return, (b) defocused image produced by applying a white phase error function.

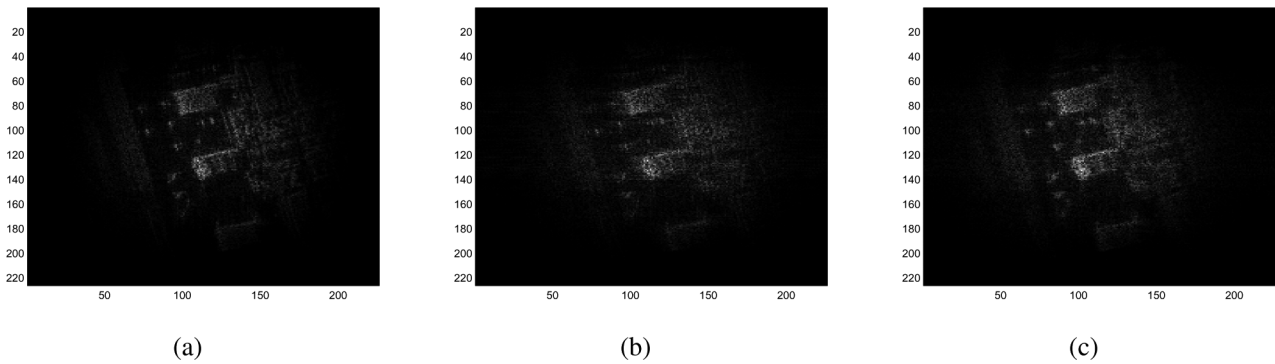


Fig. 9. Autofocus for a realistic SAR image with a 0.005 degree viewing angle: (a) image restored by FMCA, (b) image restored by MCA, (c) image restored by PGA.

can see that MCA starts to break down in this case as it depends heavily on the assumption that the collected Fourier data lie on a Cartesian grid. Note that PGA still provides a good reconstruction. The point target cross section comparison is plotted in Fig. 7(b). Note that MCA has more energy diffused outside

the point target center. Fig. 6 shows the image restoration results for a 1 degree range of viewing angles. The point target cross section comparison is plotted in Fig. 7(c). In this case, the locus of the collected Fourier data can no longer be approximated by a Cartesian grid, and MCA breaks down completely. The per-

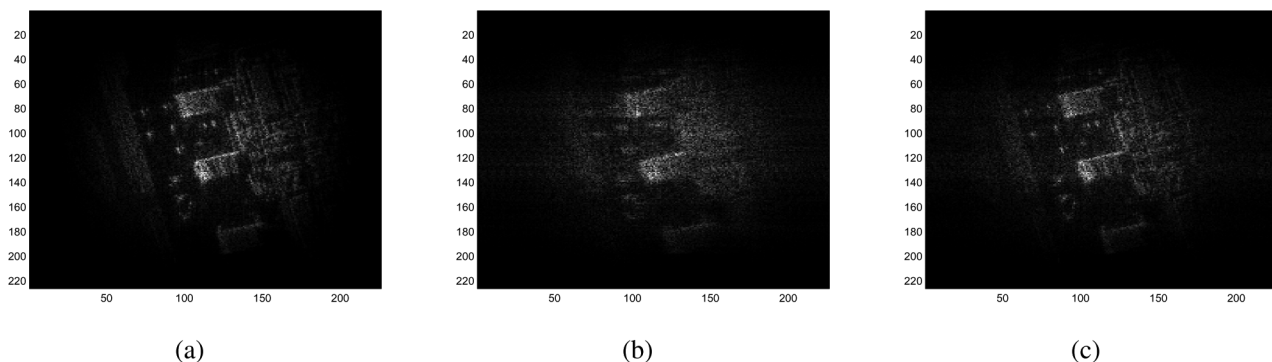


Fig. 10. Autofocus for a realistic SAR image with a 0.05 degree viewing angle: (a) image restored by FMCA, (b) image restored by MCA, (c) image restored by PGA.

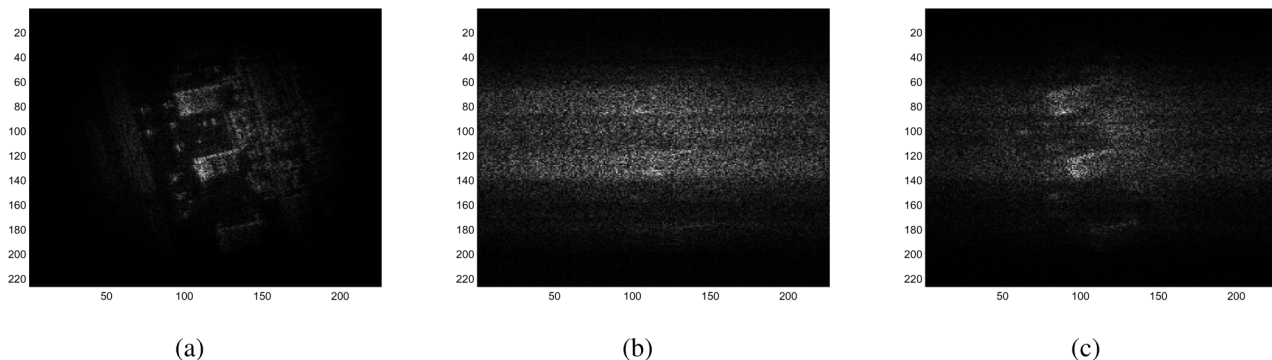


Fig. 11. Autofocus for a realistic SAR image with a 0.5 degree viewing angle: (a) image restored by FMCA, (b) image restored by MCA, (c) image restored by PGA.

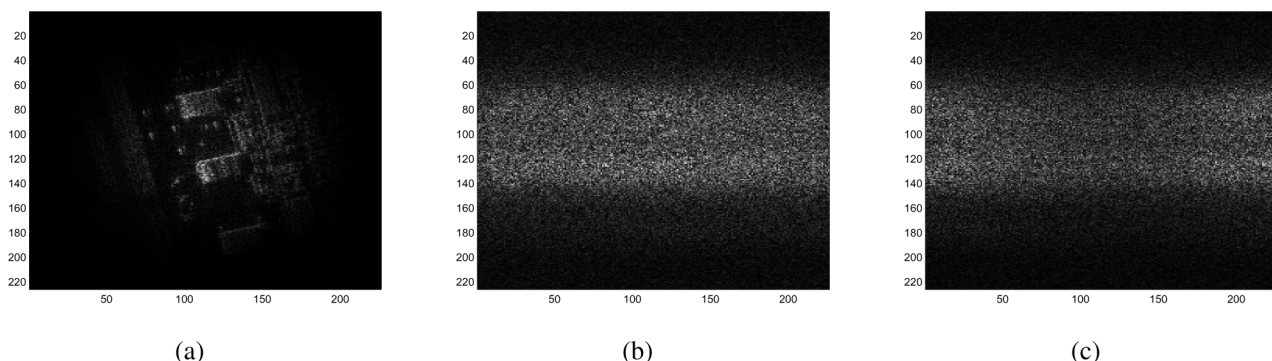


Fig. 12. Autofocus for a realistic SAR image with a 5 degree viewing angle: (a) image restored by FMCA, (b) image restored by MCA, (c) image restored by PGA.

formance degradation of PGA is also apparent as the range of viewing angles becomes wider. The performance of FMCA remains excellent as the range of viewing angles increases.

Next, we show the image restoration results for a more challenging scenario. A SAR image from Sandia National Laboratory was used as a proxy for the magnitude of a SAR scene. Again, we compare FMCA with MCA and PGA under different ranges of viewing angles. The perfectly focused image and the phase corrupted image for a 0.005 degree range of viewing angles is shown in Fig. 8 and images restored by FMCA, MCA and PGA are shown in Fig. 9. Due to the complexity of the real SAR image and by considering a white phase error function, we observe some artifacts in the PGA restoration, but otherwise PGA still produced a recognizable image. MCA performed well in this small viewing angle case. Fig. 10 shows the restoration results for a 0.05 degree viewing angle and Fig. 11 shows the restoration results for a 0.5 degree viewing angle. From these simulations, we observe that while MCA slightly outperformed

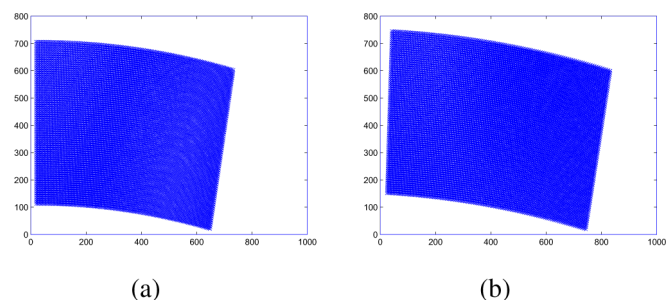


Fig. 13. Collected Fourier data pattern for bistatic SAR: (a) example for a stationary transmitter and a moving receiver, (b) example for a moving transmitter and a moving receiver.

PGA in the the smallest viewing angle case in Fig. 9, MCA breaks down more quickly when the range of viewing angles is wider. The performance of FMCA is not affected by the range of viewing angles. FMCA continued to perform well for even much wider viewing angles as seen in Fig. 12.

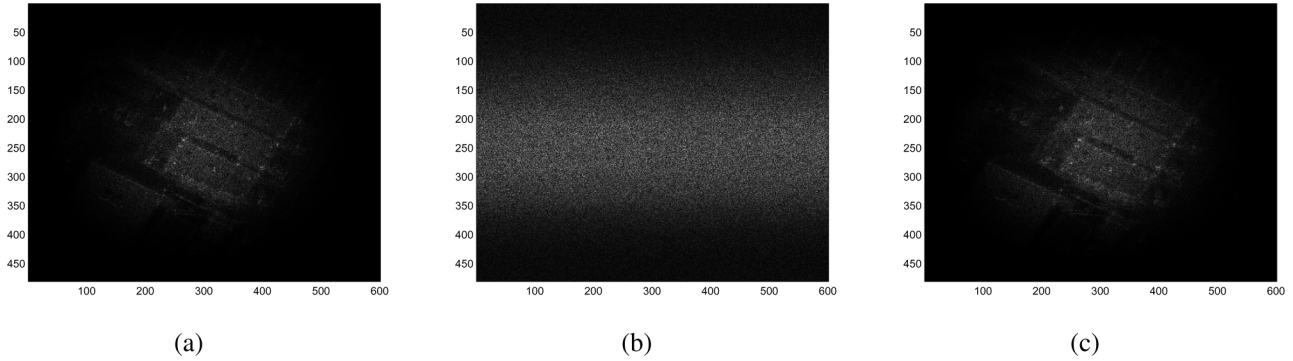


Fig. 14. Bistatic SAR autofocus for a stationary transmitter and a moving receiver: (a) perfectly-focused image, (b) defocused image produced by applying a white phase error function, and (c) image restored by FMCA.

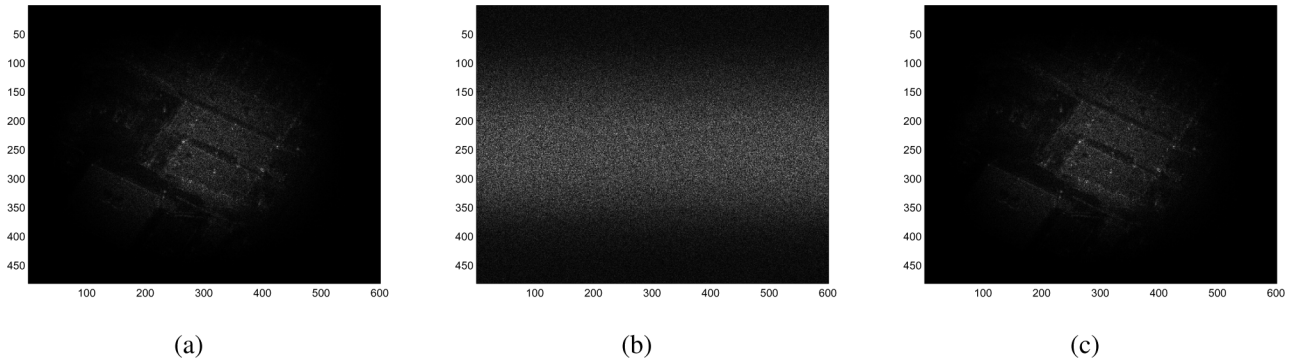


Fig. 15. Bistatic SAR autofocus for a moving transmitter and a moving receiver: (a) perfectly-focused image, (b) defocused image produced by applying a white phase error function, and (c) image restored by FMCA.

B. Bistatic SAR Scenario

Here, we demonstrate the restoration capability of FMCA for bistatic SAR. We experimented with two bistatic SAR scenarios. Scenario 1 assumed a stationary transmitter and a moving receiver; scenario 2 assumed a moving transmitter and a moving receiver with straight-line perpendicular motions. The collected Fourier data pattern for both scenarios is shown in Fig. 13. Fig. 14 shows the autofocus results for scenario 1. Fig. 15 shows the autofocus results for a scenario 2. Notice that FMCA successfully produced a focused image in both scenarios. (Neither MCA nor PGA can be applied directly to the bistatic scenario.)

VI. CONCLUSIONS

In this work, we developed a new autofocus algorithm, termed Fourier-domain multichannel autofocus (FMCA), which can accommodate both wide-angle monostatic SAR and bistatic SAR scenarios. FMCA was derived within a linear algebraic framework, allowing the autofocus phase errors to be corrected in a noniterative fashion. FMCA requires prior knowledge that a region in the underlying scene has zero or nearly-zero pixel values (low-return region). In practice, a low-return region exists in the sidelobes of the antenna pattern. The previously developed MCA approach can be viewed as a special case of FMCA when operating at very small viewing angles. We presented computer simulations to demonstrate the performance of FMCA compared to MCA and PGA for various ranges of viewing angles, and also considered bistatic SAR scenarios. In further research, we are working to characterize the sensitivity associated with the low-return assumption, and studying methods to reduce this sensitivity.

REFERENCES

- [1] D. C. Munson Jr., J. D. O'Brien, and W. K. Jenkins, "A tomographic formulation of spotlight-mode synthetic aperture radar," *Proc. IEEE*, vol. 71, pp. 917–925, Aug. 1983.
- [2] C. V. Jakowatz Jr., D. E. Wahl, P. H. Eichel, D. C. Ghiglia, and P. A. Thompson, *Spotlight-Mode Synthetic Aperture Radar: A Signal Processing Approach*. Norwell, MA: Kluwer, 1996.
- [3] P. H. Eichel, D. C. Ghiglia, C. V. Jakowatz Jr., and D. E. Wahl, "Phase-gradient autofocus for SAR phase correction: Explanation and demonstration of algorithmic steps," in *Proc. Digital Signal Processing Workshop at Starved Rock State Park*, New York, 1992, pp. 6.6.1–6.6.2.
- [4] C. V. Jakowatz Jr. and D. E. Wahl, "Eigenvector method for maximum-likelihood estimation of phase error in synthetic-aperture-radar imagery," *J. Opt. Soc. Amer.*, vol. 10, no. 12, pp. 2539–2546, Dec. 1993.
- [5] R. L. Morrison Jr., M. N. Do, and D. C. Munson Jr., "MCA: A multichannel approach to SAR autofocus," *IEEE Trans. Image Process.*, vol. 18, no. 4, pp. 840–853, Apr. 2009.
- [6] H. Cho and D. C. Munson Jr., "Overcoming polar-format issues in multichannel SAR autofocus," in *Proc. 42nd Asilomar Conf. Signals, Systems Computers*, 2008, pp. 523–527.
- [7] T. J. Kragh, "Monotonic iterative algorithm for minimum-entropy autofocus," in *Proc. Adaptive Sensor Array Processing Workshop*, Jun. 6–7, 2006.
- [8] L. Xi, L. Guosui, and J. Ni, "Autofocusing of ISAR images based on entropy minimization," *IEEE Trans. Aerosp. Electron. Syst.*, vol. 35, no. 4, pp. 1240–1252, Oct. 1999.
- [9] F. Berizzi and G. Corsini, "Autofocusing of inverse synthetic aperture radar images using contrast optimization," *IEEE Trans. Aerosp. Electron. Syst.*, vol. 32, no. 3, pp. 1185–1191, Jul. 1996.
- [10] J. R. Fienup and J. J. Miller, "Aberration correction by maximizing generalized sharpness metrics," *Opt. Soc. Amer.*, vol. 20, no. 4, pp. 609–620, 2003.
- [11] R. L. Morrison Jr. and M. N. Do, "A multichannel approach to metric-based SAR autofocus," in *Proc. IEEE Int. Conf. Image Process.*, 2005, vol. 2, pp. 1070–1073.
- [12] L. Tong and S. Perreau, "Multichannel blind identification: From subspace to maximum likelihood methods," *Proc. IEEE*, vol. 86, no. 10, pp. 1951–1968, Oct. 1998.

- [13] M. Gurelli and C. Nikias, "EVAM: An eigenvector-based algorithm for multichannel blind deconvolution of input colored signals," *IEEE Trans. Signal Process.*, vol. 43, no. 1, pp. 134–149, Jan. 1995.
- [14] G. Hari Kumar and Y. Bresler, "Blind restoration of images blurred by multiple filters: Theory and efficient algorithms," *IEEE Trans. Image Process.*, vol. 8, no. 2, pp. 202–219, Jun. 1999.
- [15] K. Liu and D. C. Munson Jr., "Fourier-domain multichannel autofocus for synthetic aperture radar," in *Proc. 42nd Asilomar Conf. Signals, Syst. Comput.*, Oct. 2008, pp. 848–852.
- [16] O. Arikan and D. C. Munson Jr., "A tomographic formulation of bistatic synthetic aperture radar," in *Proc. Int. Conf. Adv. Commun. Contr. Syst.*, 1988, pp. 289–302.



Kuang-Hung Liu (M'08) was born in Taipei, Taiwan in 1981. He received the B.S. degree in computer science and information engineering from the National Taipei University of Technology in 2003, and the M.S. degrees in electrical engineering from the University of Michigan at Ann Arbor in 2007, where he is currently pursuing the doctoral degree.

His research interests include statistical signal processing, convex optimization and applications to remote-sensing imaging.



David C. Munson, Jr. (S'74–M'79–SM'84–F'91) received his B.S. degree from the University of Delaware in 1975, and M.S., M.A. and Ph.D. degrees in 1978, 1978, and 1979, respectively, from Princeton University.

He is the Robert J. Vlasic Dean of Engineering and Professor of Electrical Engineering and Computer Science at the University of Michigan since 2006. He served as Chair of Electrical Engineering and Computer Science from 2003–2006. He served on the faculty of the University of Illinois from 1979–2003, where he was the Robert MacClimbie Distinguished Professor of Electrical and Computer Engineering. He conducts research in the area of signal and image processing, with a specialty in synthetic aperture radar.

Dr. Munson is a Fellow of the IEEE, a past president of the IEEE Signal Processing Society, founding editor-in-chief of the IEEE TRANSACTIONS ON IMAGE PROCESSING, and co-founder of the IEEE International Conference on Image Processing. In addition to multiple teaching awards and other honors, he was presented the Society Award of the IEEE Signal Processing Society and he was the Texas Instruments Distinguished Visiting Professor at Rice University. He is coauthor of multiple textbooks, including "Engineering Our Digital Future," which is introducing engineering to hundreds of high schools nationwide via the Infinity Project. He is co-founder of InstaRecon, Inc., which is commercializing fast algorithms for image formation in computer tomography.